6

Modelling Dynamics of Valley Glaciers

Surendra Adhikari and Shawn J. Marshall
Department of Geography, University of Calgary
Canada

1. Introduction

Ever since the Paleoproterozoic snowball Earth era, ca. 2.4 billion years ago (e.g. Hoffman & Schrag, 2000; Kirschvink, 1992), and beyond, the landscape of the planet Earth has been shaped up by the tremendous amount of scouring due to the repeated waxing and waning of ice masses. Over time, the dynamics of ice masses – a major part of Earth's cryosphere – has played a crucial role in global climate through complex interactions and feedbacks between the atmosphere, biosphere, and oceans. The cryosphere remains as one of the major dynamical components of the Earth system, participating in the geomorphologic and climatic evolution of the planet.

Presently, glaciers and ice sheets occupy ca. 10% of the Earth's land surface in the annual mean (Lemke et al., 2007). If it were to melt out completely, the mean sea level would rise by more than 64 m. The majority of this contribution comes from the large ice sheets of Antarctica, 56.6 m (Lythe et al., 2001), and Greenland, 7.3 m (Bamber et al., 2001). Glaciers and ice caps outside of Greenland and Antarctica contribute in a range between 0.15 m (Ohmura, 2004) and 0.37 m (Dyurgerov & Meier, 2005). In the ongoing warm epoch of climate since the little ice age, beginning in the late 19^{th} century, glaciers and ice sheets have been retreating in most regions of the world (e.g. Cook et al., 2005; Krabill et al., 1999; Zemp et al., 2006). Such a response of the cryosphere creates a high-degree of disequilibrium, with positive feedbacks on the Earth's climate system, whereby the planet is likely to face ongoing and accelerated ice loss. Giving proper attention to the cryospheric component of climate system, most climate models forecast continued warming and glacier retreat at least until the end of 21^{st} century (e.g. Christensen et al., 2007; Gillett et al., 2011).

On this premise, glaciological studies bear a tremendous importance; they are useful, for instance, (1) to understand the complex interaction between the ice and climate (e.g. Goelzer et al., 2011; Kaser, 2001), (2) to trace out the past climatic signals (e.g. Oerlemans, 2005; Thompson et al., 2003), (3) to assess the glacier-related hazards (e.g. Allen et al., 2009), and (4) to estimate glacial contributions to sea level rise (e.g. Leclercq et al., 2011; Meier, 1984; Raper & Braithwaite, 2006). To make future projections and to understand the intrinsic dynamical phenomena underlying glacier-climate interactions, such as the thermomechanical evolution of ice masses, numerical modelling, supplemented by field data, is the only option.

In this chapter, we discuss the physics and numerics of ice flow models with various degrees of complexity and we simulate the corresponding dynamics of a valley glacier. While valley glaciers make up only a tiny fraction ($< 1.0\%$) of the global cryosphere, proper understanding of glacier dynamics is essential for several reasons. First, valley glaciers are in close proximity

to human settlement; any alteration in their dynamics affects society immediately. Second, valley glaciers and ice caps are of significant concern for watershed- and regional-scale water resources (e.g. Jansson et al., 2003; Viviroli et al., 2003); they, for instance, provide fresh water supply for municipal, agricultural, and industrial purposes. Third, the dynamical response of glaciers leaves footprints of past climate in their moraines (e.g. Beedle et al., 2009); they have hence become proven indicators of climate change. More importantly, the ice flow in valley glaciers and icefields comprises a high degree of complexity, primarily due to the irregular valley geometry. This demands a high-order treatment of glacier dynamics, thereby posing a challenge to numerical modellers. Finally, the fundamental physics of glaciers (i.e. mechanisms of ice flow) do not differ from those of larger ice sheets; experience in modelling valley-glacier dynamics can be directly extended to modelling of continental-scale ice sheets.

This chapter is hence designed to focus on the dynamics of valley glacier and its modelling. We (1) introduce ice rheology and briefly summarize the history of numerical modelling in glaciology, (2) describe the model physics and analyze the various approximations associated with the low-order (reduced) models, (3) provide an overview of numerical methods, concentrating on the finite element approach, and (4) present a numerical comparison of several models with various degrees of sophistication.

2. Ice rheology and glacier modelling

The rheological properties of glacier ice are practically independent of the isotropic pressure (e.g. Rigsby, 1958), and are therefore commonly described using deviatoric stresses rather than Cauchy stresses. The constitutive equation that relates deviatoric stresses to strain-rates in randomly oriented polycrystalline ice (under secondary creep) is given by the linearized inversion of Glen's flow law (Glen, 1955), i.e.

$$\tau_{ij} = 2\eta\dot{\epsilon}_{ij}, \tag{1}$$

where τ is the deviatoric stress tensor, $\dot{\epsilon}$ is the strain-rate tensor, and η is the effective viscosity. The viscosity of glacier ice is strain-rate dependent and is given by,

$$\eta = \frac{1}{2}A^{-\frac{1}{n}}\dot{\epsilon}_e^{\left(\frac{1-n}{n}\right)}, \tag{2}$$

where A is the flow law rate factor, n is the flow law exponent, and $\dot{\epsilon}_e$ is the effective strain-rate that can be understood from the second invariant of $\dot{\epsilon}$, i.e.

$$2\dot{\epsilon}_e^2 = \dot{\epsilon}_{ij}\dot{\epsilon}_{ji}. \tag{3}$$

By defining

$$\dot{\epsilon}_{ij} = \frac{1}{2}(u_{i,j} + u_{j,i}), \tag{4}$$

deviatoric stresses in Equation (1) can easily be expressed in terms of ice velocity, u, – the readily observable glaciological field variable.

Hypotheses and experimental foundations of this theory of ice rheology are given by Glen (1958) and are reviewed in detail by, e.g. Alley (1992), Budd & Jacka (1989), Cuffey & Paterson (2010), Hooke (1981), and Marshall (2005). Since the form of the constitutive relation (Eq. 1) is well-established and can be explained in terms of dislocation theory, these discussions revolve around the suitable parameterizations of A and n. The flow law rate factor, A, is

thought to depend primarily on ice temperature, as well as on crystal size and orientation (anisotropy), water and impurity content, ice density and pressure, and perhaps on other several factors. Only the thermal dependence of A has been parameterized, following an Arrhenius relation (e.g. Hooke, 1981; Paterson & Budd, 1982), and coupled successfully with dynamical ice-flow models (e.g. Huybrechts & Oerlemans, 1988; Marshall & Clarke, 1997). Several attempts have also been made to account for anisotropic effects through the introduction of a "flow enhancement factor", both empirically (e.g. Wang & Warner, 1999) and through physically-based parameterizations (e.g. Gillet-Chaulet et al., 2005; Morland & Staroszczyk, 2003).

Similarly, the choice of flow law exponent, n, is also not obvious, as it varies in a range $1.5 - 4.2$ under different stress regimes (Weertman, 1973). For the realistic scenarios, i.e. $\tau \approx 50 - 200$ kPa, $n = 3$ is representative (e.g. Cuffey & Paterson, 2010). Assuming isothermal and isotropic ice masses for purposes here, we use $n = 3$ and $A = 10^{-16}$ Pa^{-3} a^{-1} as in, e.g. Pattyn et al. (2008) and Sargent & Fastook (2010).

In the early 1950s, the power-law relation between τ and $\dot{\epsilon}$ (Eqs. 1–3) was formulated based on laboratory experiments (Glen, 1952) and field observations on the closure of boreholes (Nye, 1953). Subsequently, the Glen-Nye law, commonly known as the Glen's law after Glen (1955), emerged to describe the glacier ice as a quasi-viscous fluid with non-Newtonian flow behaviour. This not only discarded the then-prevailing theory of "extrusion flow" (see Waddington, 2010), but also opened the door for investigating the theoretical and mathematical foundations of modern glaciology. Nye's works (e.g. Nye, 1952; 1959) mark the beginning of such investigations, particularly focusing on the motion of glacier ice. Robin (1955) was the first to calculate ice temperature by considering glacial thermodynamics. Due to the lack of computational power, these early works were primarily based on the semi-analytical methods used in contemporary fluid mechanics. A nice summary of these early works that form the foundation of physical glaciology is given in Clarke (1987).

With the dawn of digital computing, model-based studies of glacier dynamics started in late 1960s (e.g. Campbell & Rasmussen, 1969). Soon after, several numerical models (e.g. Budd & Jenssen, 1975; Mahaffy, 1976; Oerlemans, 1982) were developed, including the ones with thermomechanical coupling (e.g. Jenssen, 1977). These pioneer models were based on the "shallow-ice" theory of glacier mechanics (e.g. Nye, 1959), which assumes that ice thickness is much less than the horizontal length scale over which a domain is discretized. This theory was later developed rigorously by Hutter (1983) and Morland (1984), which is now known formally as the shallow-ice approximation (SIA). SIA models have been used extensively for simulating large ice sheets (e.g. Calov & Hutter, 1996; Huybrechts & Oerlemans, 1988), as well as valley glaciers (e.g. Adhikari & Huybrechts, 2009; Oerlemans et al., 1998). In general, ice sheet models need to thermomechanically coupled, since the polar ice sheets span a range of temperature from the melting point to ca. –50°C, whereas models for temperate valley glaciers are commonly isothermal. This is reasonable outside of the polar regions, as most of the world's valley glaciers are temperate: at the pressure-melting point throughout. For SIA models with and without the coupled thermodynamics, benchmark numerical experiments are presented respectively by Payne et al. (1996) and Huybrechts et al. (1996).

SIA theory is strictly valid only where horizontal gradients in ice thickness and velocity are negligibly small and bedrock slopes are sufficiently gentle. These criteria are clearly violated in valley glaciers (e.g. Le Meur et al., 2004; Leysinger Vieli & Gudmundsson, 2004),

fast-flowing ice streams (e.g. Whillans & Van der Veen, 1997), and at the ice divides and grounding zones of ice-sheet/ice-shelf systems (e.g. Baral et al., 2001). Several attempts have therefore been made to capture high-order dynamics in ice flow models; effects of longitudinal stress gradients (e.g. Adhikari & Marshall, 2011; Shoemaker & Morland, 1984; Souček & Martinec, 2008) and lateral drag (e.g. Adhikari & Marshall, in preperation; Nye, 1965) are particularly accounted via physically-based or numerical/empirical parameterizations. More complete representations of glacier dynamics are provided by high-order (e.g. Blatter, 1995; Pattyn, 2003) and Stokes (e.g. Jarosch, 2008; Jouvet et al., 2008; Zwinger et al., 2007) models. The development history of such models is nicely summarized by Blatter et al. (2010); corresponding benchmark experiments are presented by Pattyn et al. (2008).

With the material nonlinearity (see Eqs. 1–2), even SIA models are not analytically tractable; the coupled evolution of glacier temperatures, rheology, and high-order velocities therefore requires a numerical solution. A few attempts have been made to obtain analytical solutions (e.g. Bueler et al., 2007; Sargent & Fastook, 2010), however, at least as a tool for verification of numerical models in simple geometric and climatic settings.

3. Model physics, approximations, and boundary conditions

For full simulations of Earth's climate system, the dynamical models of glaciers and ice sheets are coupled with those of other climatic components, namely the atmosphere, the biosphere, and the ocean (see, for example, Fig. 1 in Huybrechts et al., 2011). The models of glaciers and ice sheets are usually accompanied by, for instance, (1) a mass balance model that describes the physics of mass exchange at the ice/atmosphere and ice/ocean interface, (2) a model of glacial isostatic processes whereby the underlying bed deforms due to the load of ice, and (3) a model of subglacial till deformation that yields the associated basal motion of ice. The intrinsic processes of ice flow can be described by a combination of gravitational creep deformation and decoupled basal sliding. To simulate creep deformation (i.e. effective viscosity) and to predict the regions where ice masses are warm-based (permitting basal sliding), a proper account of energy balance is essential. Along with the companion models listed above, a full three-dimensional ice flow model, equipped with thermomechanical coupling, is therefore required for the realistic simulations of glacier dynamics.

We outline a simple flowchart (Fig. 1) depicting the major components of a typical ice flow model. Given the boundary conditions and some description of mass budget, we accomplish ice flow modelling in a two-step simulation: (1) diagnostic simulation of a set of steady-state problems in order to obtain the quasi-stationary englacial velocity/stress and temperature fields at time t, and (2) prognostic simulation satisfying kinematic boundary conditions to update the glacier geometry at a subsequent time, $t + \Delta t$. Below, we describe the physics and associated low-order approximations of several ice flow models.

3.1 Diagnostic equations

Dynamical models for ice flow are based on the fundamental physics of conservation of mass, momentum, and energy. Glacier velocities are so small that we can remove the acceleration term from the momentum balance equation; the dynamical problem in glaciology therefore reduces to a Stokes problem. For isothermal glacier domains in $k(\geq 2)$-dimensional Euclidean

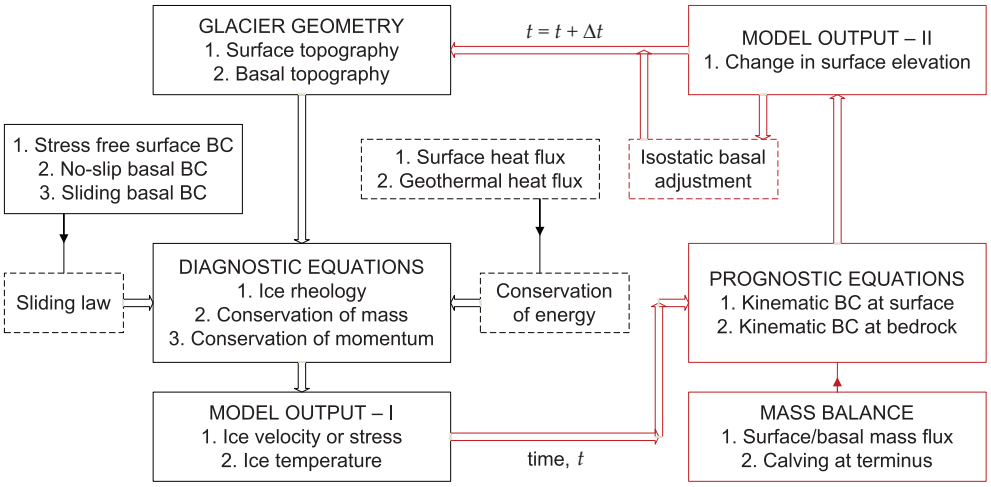

Fig. 1. Flowchart of an ice flow model. The processes associated with the diagnostic and prognostic simulations are listed in the LHS and RHS boxes, respectively; black and red colors are used for clarity. Dotted boxes enclose the processes that are not considered in this study. Mid-arrows are used to depict the corresponding boundary conditions.

space, $\Re^k$, the Stokes problem can be stated as,

$$u_{i,i} = 0, \tag{5}$$

$$\sigma_{ij,j} + \rho g_i = 0, \tag{6}$$

where u is the velocity vector, σ is the Cauchy stress tensor, ρ is ice density, and g is the gravity vector. We split σ into its deviatoric part, τ, and an isotropic pressure, p, i.e.

$$\sigma_{ij} = \tau_{ij} + p\delta_{ij}, \tag{7}$$

whereby the momentum balance equation (Eq. 6) can be expressed in terms of the velocity vector, as explained in Section 2. The isotropic pressure is dependent on the trace of Cauchy stress tensor, i.e. $p = \sigma_{ii}/k$, and is activated via the Kronecker delta, δ_{ij}, only when normal stresses are being considered ($\delta_{ij} = 1$ for $i = j$, and $\delta_{ij} = 0$ otherwise).

Intuitively, three-dimensional (3D) Stokes models, which solve a complete set of Stokes equations (Eqs. 5–6), describe the most sophisticated treatment of glacier dynamics. Virtually all models developed to date (e.g. SIA or high-order) can be considered as approximations of a Stokes model. Hindmarsh (2004) compares the numerical solutions of various approximations to the Stokes equations. Apart from the standard SIA model, he considers an 'L' family of models that include some of most common models, such as those of Blatter (1995), MacAyeal (1989) and Pattyn (2003). These L-models differ from each other in: (1) how they reduce the definitions of momentum balance (Eq. 6), strain-rate tensor (Eq. 4) and its second invariant (Eq. 3), and (2) how they obtain the approximate solutions of ice velocities from the previous iteration step to calculate effective viscosity (Eq. 2). Since such approximations are made primarily to optimize the solution accuracy and computational efficiency, it is not always obvious how to choose a particular model for a given glaciological scenario. Here, we present

new brands of models, whose associated approximations clearly define the distinct physical mechanisms of glacier dynamics; the scope of each model therefore becomes apparent.

In a 3D domain of land-based glacier, key physical processes that act to balance a gravity-driven ice-flow consist of basal drag, τ_b, resistance associated with longitudinal stress gradients, τ_{lon}, and lateral drag, τ_{lat}. Mathematical details of these resistances can be found, for example, in Van der Veen (1999) and Whillans (1987). Based on the physical mechanisms associated with each resistance, we define three families of models. Ice flow in the first family of models is controlled collectively by $(\tau_b + \tau_{lon} + \tau_{lat})$, in the second one by $(\tau_b + \tau_{lon})$ only, and in the third one by τ_b alone. For a fairly wide glacier (such that $\tau_{lat} \approx 0$) resting on steep and undulating bedrock (such that τ_{lon} is significant), for example, the second family of models should be optimal to yield realistic simulations. Members of a given model family differ from each other mainly in that they deal with different spatial dimensions. Below, we describe each of them; relevant governing equations are given in Appendix A.

3.1.1 Full-system Stokes (FS) model

If a model solves the Stokes equations (Eqs. 5–6) in 3D space, $\Re^3$, we call it the full-system Stokes model (FS). This is the only member of the first model family. Here, the indices (i, j) refer to Cartesian coordinates (x, y, z); x is the horizontal coordinate along the principal flow direction, y is the second horizontal coordinate along the lateral direction, and z is the vertical coordinate opposite to gravity.

3.1.2 Plane-strain Stokes (PS) model

The 3D plane-strain Stokes model (PS3) does not strictly follow the plane-strain approximations as its name suggests. It rather excludes the lateral gradients of stress deviators, i.e. $\tau_{ij,y} = 0$, in the momentum balance equation (Eq. 6), and those of ice velocities, i.e. $u_{i,y} = 0$, in the strain-rate definition (Eq. 4). The flowline version of this model (PS2) solves the Stokes equations in a two-dimensional (2D) space, $\Re^2$, and hence follows the plane-strain approximations. In a flowline model, the indices (i, j) refer to Cartesian coordinates (x, z), where x and z are once again the horizontal and vertical coordinates, respectively.

3.1.3 Shear-deformational (SD) model

In 3D shear-deformational model (SD3), the vertical shear stresses, i.e. τ_{iz} with $i = (x, y)$, are the only non-zero stress components. As for the PS3 model, it also excludes the lateral gradients of stress deviators and ice velocities. In its flowline counterpart (SD2), τ_{xz} is the only non-zero stress component; no further assumption is needed.

The standard zeroth-order SIA models (Hutter, 1983) also belong to the SD family. The three-dimensional (SIA3) and flowline (SIA2) shallow-ice models can be derived respectively from the SD3 and SD2 models, by further assuming that the horizontal gradients in vertical shear stresses and ice velocities are negligible, i.e. $\tau_{iz,x} = 0$ and $u_{i,x} = 0$. The laminar-flow model (LF) is the simplest of SD models. There exist analytical solutions for ice velocities in isothermal, laminar flow (e.g. Cuffey & Paterson, 2010; Van der Veen, 1999); the horizontal velocity, u_x, at any point on the flowline plane (x, z), for example, is given by

$$u_x(x,z) = u_x(x,b) + \frac{2A}{n+1}\left[\rho g_z \alpha_s(x)\right]^n h(x)^{n+1}\left[1 - \left(\frac{s-z}{h(x)}\right)^{n+1}\right], \tag{8}$$

where $u_x(x,z)$ and $u_x(x,b)$ are respectively the velocities at any depth z and at the bedrock $z = b$. Similarly, g_z is the vertical component of the gravity vector, $h(x)$ is the ice thickness, s is the glacier surface, and $\alpha_s(x)$ is the surface slope.

3.2 Prognostic equations

In prognostic simulations of each model, the glacier surface, $z = s$, evolves satisfying the kinematic boundary condition,

$$s_{,t} + u_i(s)s_{,i} = u_z(s) + m(s,t), \tag{9}$$

where subscript t represents time, index i refers to the horizontal coordinates, i.e. $i = (x,y) \subset \Re^3$, and $i = x \subset \Re^2$, $u_z(s)$ is the vertical velocity at the glacier surface, and m is the mass balance function. To compute the unknown s at a new time $t + \Delta t$, we obtain glacier surface velocities from the diagnostic simulation of domain at an antecedent time t, and prescribe $m(s,t)$ as a vertical flux with units m ice eq. a^{-1}.

3.3 Boundary conditions

In addition to the kinematic boundary condition (Eq. 9), the upper ice surface satisfies the stress free criterion, i.e. $\sigma_{ij}(s) \approx 0$. This involves an assumption that the role of atmospheric pressure on the overall dynamics of glacier ice is negligibly small. The kinematic boundary condition (similar to Eq. 9) is also applied at the ice/bedrock interface. However, we impose a no-slip basal criterion, i.e. $u_i(b) = 0$. In doing so, we assume no mass exchange due to ice melting/refreezing, i.e. $m(b,t) = 0$, thus restricting the evolution of basal ice, i.e. $b_{,t} = 0$.

The lateral boundary condition (glacier margin) is typically free in glacier simulations, with ice free to advance or retreat within a domain. Domain extent is designed such that the ice mass does not reach the boundary; it then freely evolves within the domain, with a zone with ice thickness $h = 0$ around the periphery. If the combined snow accumulation rates and ice flux into an empty grid cell exceed local mass loss (ablation), the grid cell becomes glacierized and is included in the overall glacier continuum.

4. Numerical methods applied to glacier dynamics

The existence of numerical solutions to strongly nonlinear Stokes problem discussed in Section 3.1 is proven in Colinge & Rappaz (1999). Various approaches have been used to obtain solutions in 3D space; numerical schemes such as finite difference (e.g. Colinge & Blatter, 1998; Huybrechts et al., 1996; Marshall & Clarke, 1997; Pattyn, 2003), finite element (e.g. Gudmundsson, 1999; Hanson, 1995; Jarosch, 2008; Jouvet et al., 2008; Picasso et al., 2008; Zwinger et al., 2007), control volume (e.g. Price et al., 2007), and spectral (e.g. Hindmarsh, 2004) methods have all been employed. Finite difference (FD) and finite element (FE) methods are more common; we use the latter one. Along with a brief overview of the FD method, below we provide theoretical and numerical details of the FE method.

4.1 Finite difference method (FDM)

Most "classical" models of glacier and ice sheet dynamics are based on FDM, where the 3D domain is split into a series of regular grid cells on a Cartesian or spherical (i.e. Earth) grid. Staggered grids are used, solving ice thickness, stress and temperature in the cell centre and

3D velocity fields at the cell interfaces, with discretization of the governing equations through standard second-order FD approximations (e.g. Huybrechts & Oerlemans, 1988). Vertical resolution is usually fine compared to horizontal resolution, with 10-40 layers in the vertical, on an adaptive, stretched grid that is updated each time step as the glacier thins or thickens. Sometimes a nonlinear vertical grid transformation is also introduced in order to increase resolution near the bed, where velocity gradients are strongest.

For SIA models, the system of FD equations is particularly efficient to solve, as the governing equation at a point is dependent on only local conditions (ice thickness, surface slope). In this case the solution depends only on the nearest neighbours to a grid cell, presenting a banded matrix system that is amenable to sparse matrix techniques. With a more complete representation of the physics, i.e. the Stokes and high-order models, solutions are non-local and computational costs increase by at an order of magnitude or more (Blatter, 1995).

FD discretizations are also limited in their ability to describe complex geometries, as found in valley glaciers, ice shelves, and fjords: many of the most interesting glaciological situations. Much of the most interesting dynamics is at the glacier or ice sheet margin, where increased resolution is desirable. We therefore turn to FE method for glaciological simulations for the remainder of this chapter.

4.2 Finite element method (FEM)

The existence and convergence of FE solutions for the glaciological (Stokes) problem have been proven in Chow et al. (2004) and Glowinski & Rappaz (2003). Let $\Omega \in \Re^k | k \geq 2$ be a continuous glacier domain, enclosed by a boundary Γ. In FE schemes, we decompose Ω into a finite number of elemental domains Ω_e, thereby generating a finite number of boundary domains Γ_e. Satisfying the relevant boundary conditions, we first seek the approximate solutions of field variables within each sub-domain, Ω_e. We then assemble them over the continuous domain, Ω, to obtain the required solutions.

There are several methods, such as variational and weighted residuals, to formulate the FE counterparts of the governing equations. We use the standard Galerkin method – a weighted residual approach in which the weighted sum of system residuals arising from the FE approximations of a continuous domain is set to zero.

4.2.1 Diagnostic equations

Let $\tilde{u}$ and $\tilde{p}$ be the approximate solutions of field variables that vary within Ω_e, according to the respective interpolation functions ψ^u and ψ^p, such that

$$\tilde{u}(x,y,z) = \psi_i^u(x,y,z)u_i = [\psi^u(x,y,z)]\{u\}, \tag{10}$$

$$\tilde{p}(x,y,z) = \psi_i^p(x,y,z)p_i = [\psi^p(x,y,z)]\{p\}, \tag{11}$$

where index i refers to the elemental degrees of freedom associated with the velocity vector and pressure, respectively. Hence, $\{u\}$ and $\{p\}$ denote the nodal velocities and pressure.

By plugging in the approximations of field variables (Eqs. 10–11), we obtain the residuals of the diagnostic equations presented in Section 3.1. The weighted sum of these residuals,

according to the standard Galerkin method, is then set to zero, i.e.

$$\int_{\Omega_e} \psi^p \left[\tilde{u}_{i,i}\right] \, \mathrm{d}\Omega_e = 0, \tag{12}$$

$$\int_{\Omega_e} \psi^u \left[\sigma_{ij,j}(\tilde{u}_i, \tilde{p}) + \rho g_i\right] \, \mathrm{d}\Omega_e = 0. \tag{13}$$

Here the weights are chosen to be the assumed interpolation functions; this is unique to the Galerkin method (e.g. Rao, 2005). See Appendix B for the details of construction of a linear system of these equations in 3D Cartesian coordinates.

As the governing equations comprise a one-degree high-order of derivative for the velocity vector than that for the isotropic pressure (see Appendix A), a typical Taylor-Hood element (Hood & Taylor, 1974) with quadratic interpolation function for velocities and linear one for pressure is recommended. For simplicity, however, we use the same order of interpolation function, so that $\psi^u = \psi^p \equiv \psi$. Any instability arising as a result is accommodated by using the stabilized finite elements (Franca & Frey, 1992).

Stabilization involves addition of mesh-dependent terms to the Galerkin formulation. These additional terms are the Euler-Lagrange equations evaluated elementwise, so that exact solutions satisfy both the Galerkin and these additional terms. The additional terms are,

$$\left\langle \sigma_{ij,j}, \delta_1 \sigma_{ij,j} \right\rangle + \left\langle u_{i,i}, \delta_2 u_{i,i} \right\rangle, \tag{14}$$

$$\left\langle \rho g_i, \delta_1 \sigma_{ij,j} \right\rangle. \tag{15}$$

Equation (14) is added to the elemental coefficient matrix and Equation (15) is added to the RHS force vector. In Equation (14), the first term inside the first inner product is the residual of momentum balance equation (Eq. 13), excluding the force term, and the first term inside the second inner product is the residual of continuity equation (Eq. 12). The second terms associated with stability parameters δ_1 and δ_2 are the stabilization contributions to the weight functions. Here, these contributions are assumed to be the same as the respective system residuals. The stability parameters are chosen following (Franca & Frey, 1992),

$$\delta_1 = \frac{m_k h_k^2}{4\eta}, \; \delta_2 = \frac{2\eta}{m_k}, \tag{16}$$

where m_k depends on the type of the element and h_k on its size. Details of diagnostic system stabilization (for the FS model) are given in Appendix C.

4.2.2 Prognostic equations

In prognostic simulations, we seek the approximate solution, $\tilde{s}$, of s along the ice surface. Over each relevant Γ_e, $\tilde{s}$ varies according to the chosen interpolation function ψ^s, such that

$$\tilde{s}(x, y, t) = \psi_i^s(x, y, t) s_i = \left[\psi^s(x, y, t)\right] \{s\}. \tag{17}$$

With this approximation of field variables, we obtain the residuals of the prognostic equation (Eq. 9), whose weighted sum is set to zero,

$$\int_{\Gamma_e} \psi^s \left[\tilde{s}_{,t} + u_i \tilde{s}_{,i} - (u_z + m)\right] \, \mathrm{d}\Gamma_e = 0. \tag{18}$$

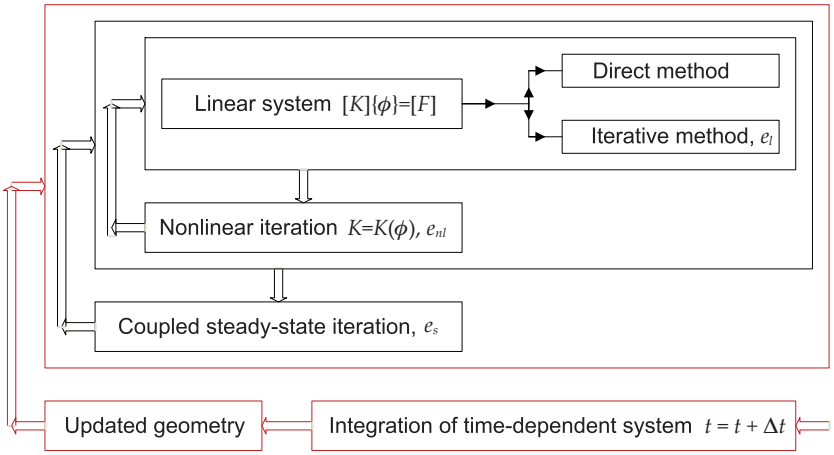

Fig. 2. Flowchart of the solution scheme. Here also, red color is used to distinguish the prognostic simulations from the diagnostic ones

This hyperbolic equation is stabilized by adding the element-wise terms (Donea & Huerta, 2003) to the mass and coefficient matrices, as well as to the force vector. Mathematical details of FE formulation and stabilization of the prognostic equation are given in Appendix D.

4.2.3 Elmer and model numerics

We use the open source FEM code Elmer (http://www.csc.fi/elmer), adapted for Glen's flow law for ice (Glen, 1955). Elmer gives approximate (numerical) solutions for both the FS and reduced models by solving the weak forms of the respective governing equations. The solutions from the FS and PS2 models are tested by Gagliardini & Zwinger (2008), against the ISMIP-HOM (Ice Sheet Model Intercomparison Project for Higher-Order Models; Pattyn et al., 2008) benchmark experiments. We solve additional subroutines to obtain FE solutions for the PS3 and SD family of models. We validate SIA2 model by comparing results with the corresponding analytical solutions (Eq. 8; see Adhikari & Marshall, 2011).

We sketch a flowchart of the solution scheme employed in Elmer (Fig. 2). The linear system of equations obtained from the Galerkin formulation (Eq. B16) is in the core of the solver. This can be solved by using either direct or iterative methods. The direct method yields an exact solution up to the machine precision; this, however, is not feasible for large problems. We therefore use an iterative method, the Krylov subspace method method (biconjugate gradient stabilized method, BiCGStab) with with an incomplete lower-upper factorization (ILU4) as the system pre-conditioner, and obtain the approximate solutions. Given the mesh density and element type, the accuracy of such solutions relies on the chosen convergence criterion, e_l; the smaller the value of e_l, the more accurate the solutions. However, too small a choice of e_l makes the job computationally inefficient.

We then solve the material nonlinearity associated with the constitutive relation. We apply a fixed point iteration scheme (the Picard linearization) to linearize the system by expressing η in terms of u_i from the previous iteration step. Here also, a suitable convergence criterion, e_{nl}, should be satisfied. For a given transient domain, we integrate the prognostic equation

until the steady-state criterion, e_s, is reached; we use implicit scheme (first-order backward differentiation formula, BDF, scheme) for such time-dependent integrations. We advise maintaining $e_l < e_{nl} < e_s$ for good convergence. Other aspects of Elmer (e.g. effects of mesh density on solution accuracy and computational efficiency, and parallel simulations) are given by Gagliardini & Zwinger (2008).

For each experiment considered in this study, we generate the structured mesh by using ElmerGrid. ElmerGrid is basically a 2D mesh generator, but is also capable of extruding and manipulating the mesh in the third dimension. Since 3D experiments require a large amount of memory and computation time, we perform parallel runs in a high-performance computing cluster provided by the Western Canadian Research Grid (WestGrid).

5. Numerical comparison of physical approximations

We consider a 10×2.5 km^2 glacial valley. To mimic a typical real-world glacier scenario, we include meanders and bumps in the subglacial topography, $b\,(x, y)$, as defined below,

$$b\,(x, y) = 5000 - x \tan \alpha_b + a_x \sin\left(0.5\pi + \frac{4\pi x}{L}\right) - a_y \sin\left[(y + \theta)\,\frac{\pi}{W}\right], \tag{19}$$

where α_b is the mean bedrock slope in radians, L and W are the longitudinal and lateral extents of the valley, a_x and a_y are the amplitudes of the topographical variation in x and y directions, and θ is the sinusoidal offset of the flowline. Here, we use $\alpha_b = 12^\circ$, $L = 10$ km, $W = 2.5$ km, $a_x = 200$ m, $a_y = (500 + 0.05x)$ m, and $\theta = 500 \sin(2\pi x/L)$ m. The plan view of basal topography is shown in Figure 3a; the central flowline is also depicted.

Next, we define the climatic regime. For $z \leq 4.6$ km and over a 500-m wide corridor around the central flowline (see Fig. 3a), the mass balance function, $m\,(s, t)$, is chosen as,

$$m(s, t) = \beta\,[s(x, y) - E] + \Delta m(t), \tag{20}$$

where β is the linear mass balance gradient, E is the equilibrium line altitude (ELA), and $\Delta m(t)$ is the time-dependent mass balance perturbation; $m\,(s, t) = 0$ elsewhere. For now, we choose $\beta = 0.01$ m ice eq. a^{-1} m^{-1}, $E = 3.7$ km, and $\Delta m(t) = 0$ m ice eq. a^{-1}. Since $s(x, y)$ evolves in prognostic simulations (Eq. 9), the parameterization of $m(s, t)$ (Eq. 20) ensures that our models capture the height/mass-balance feedback inclusively.

Under these geometric and climatic settings, we grow glaciers to steady state using several models. In order to illustrate the importance of each physical mechanism of ice flow, we consider three different models (one from each model family), namely the FS, PS3 and SIA3 models. We denote them respectively by FS, PS and SD, unless otherwise specified. Each model domain consists of 50 k bilinear quadrilateral elements, with average horizontal dimensions 50×50 m^2. The vertical dimension of element varies according to the ice thickness; we use five vertical layers. Below, we carry out numerical comparison of these 3D models in terms of steady state geometry, surface velocity, basal shear stress, and response timescales. Considering pragmatic flowline models (PS2 and SIA2), we also present a brief tutorial on modelling valley glacier dynamics, which involves (1) sensitivity tests for a glacier, (2) reconstruction of past climate or glacier extent, and (3) projection of a glacier's future.

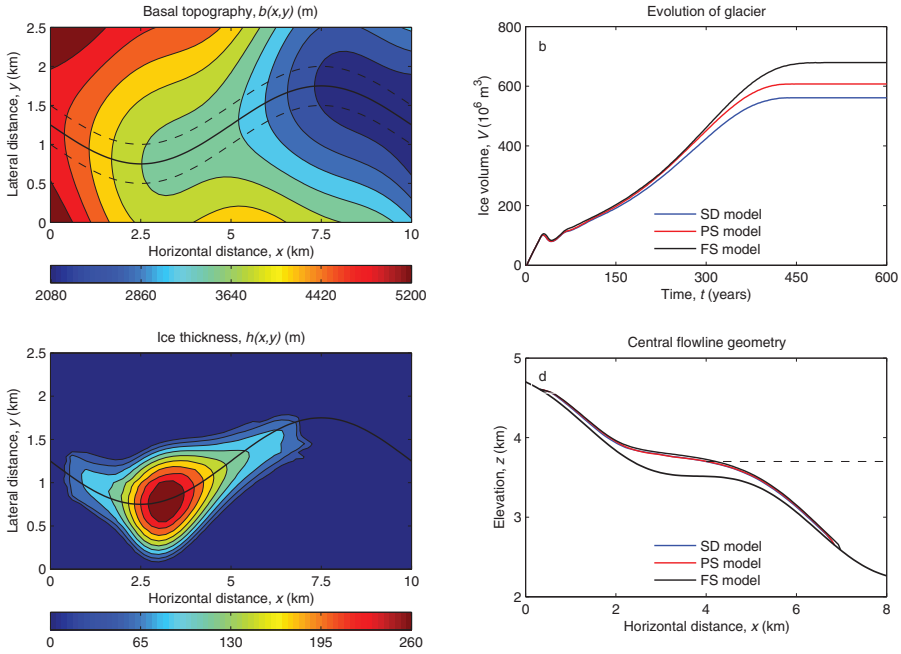

Fig. 3. (a) Basal topography, showing the central flowline. The mass balance function (Eq. 20) is applied only over a passage enclosed by dotted lines. (b) Evolution of ice volume. (c) Steady state ice thickness obtained from the FS model. (d) Longitudinal profiles of steady state geometry along the central flowline; the corresponding ELA is shown with a dotted line.

5.1 Geometry and field variables

The evolution of a glacier from zero ice volume to steady state is shown for each model case (Fig. 3b). By accounting for the high-order physical mechanisms, FS and PS models hold more ice mass than does the SD model. To assess the importance of high-order dynamics, i.e. the role of τ_{lat} and/or τ_{lon}, we compute errors between the models. We denote the error, for example, by $e_{PS.FS}$ to explain a difference between the PS and FS models with respect to the latter one. The errors $e_{PS.FS}$ and $e_{SD.PS}$ therefore illustrate the sole role of τ_{lat} and τ_{lon}, respectively; while $e_{SD.FS}$ explains their collective effects. The steady state ice volume obtained from each model and the associated errors are listed in Table 1. For the chosen geometric setting, the role of τ_{lat} ($e_{PS.FS} = -10.6\%$) is relatively more pronounced than that of τ_{lon} ($e_{SD.PS} = -7.6\%$).

The plan view of the steady state ice thickness obtained from the FS model is shown in Figure 3c. The maximum ice thickness is observed along the central flowline, and specifically around the basal depression at $x \approx 3$ km. This is true for each model case, as shown in Figure 3d. Although the longitudinal profiles of surface elevation appear to superimpose on each other, there is a considerable difference in both the mean (Table 1) and maximum values of ice thickness. The SD model generates a glacier that is 6.4% and 15.9% thinner than the PS

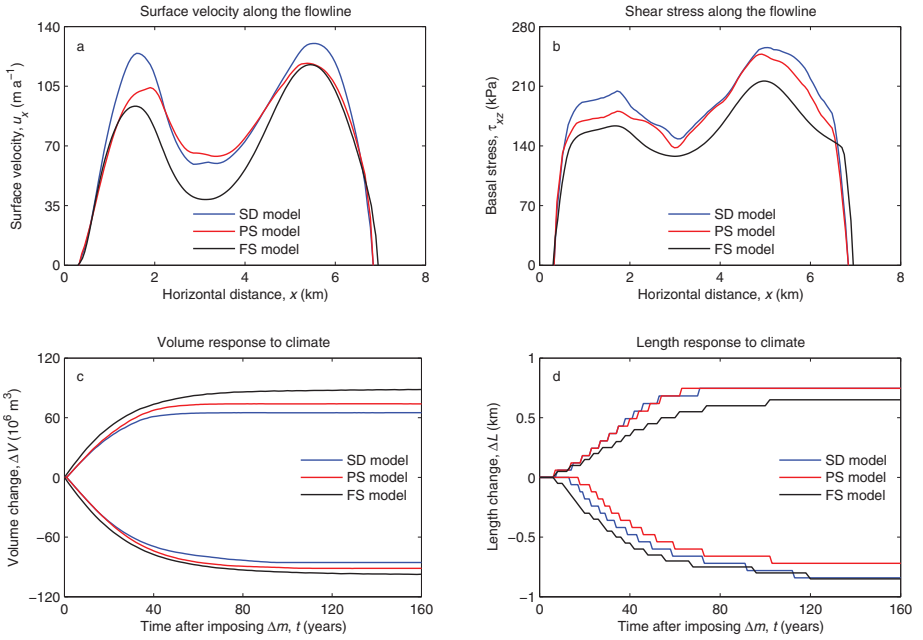

Fig. 4. (a) Surface velocity and (b) basal shear stress along the central flowline. Evolutions of (c) ice volume and (d) glacier length in response to step changes in climate, imposed on the steady-state glaciers whose geometries are shown in Fig. 3.

and FS models, respectively. This indicates the significance of resistances associated with the high-order dynamics; τ_{lat} once again appears to be more crucial than τ_{lon}.

The steady state horizontal velocity at the upper ice surface, $u_x(x, y, s)$, along the central flowline is plotted in Figure 4a. In each model case, we find smaller velocities around the basal depression at $x \approx 3$ km; while ice flows faster at places with steeper basal slopes (see Fig. 3d). Due to resistive effects of high-order dynamics, the FS and PS models yield relatively smaller ice velocities. The mean surface velocity along the central flowline in the SD model is higher by 5.9% and 23.6% than in the PS and FS models, respectively (Table 1).

We also calculate the deviatoric stresses from the englacial velocity field, using Equations (1–4). The vertical shear stress at the ice/bedrock interface, $\tau_{xz}(x, y, b)$, in a steady state longitudinal profile along the central flowline is shown in Figure 4b. As expected, basal shear stress is smaller in the PS and FS models, where other stress components are also active (i.e. τ_{xz} is not the only non-zero component) to control the glacier ice flow. In the SD model, $\tau_{xz}(x, y, b)$ characterizes τ_b (e.g. Adhikari & Marshall, 2011), which is the sole resistance to the gravitational driving stress, τ_d; it follows that $\tau_{xz}(x, y, b) \approx \tau_d$. Therefore, we calculate the errors as the difference between the SD and FS/PS models with respect to the former one. This gives a rough idea about the fractional contributions of high-order resistances, i.e. other than τ_b, to balance the gravity-driven ice flow; we find $\tau_{lon} \approx e_{SD.PS} = 6.1\%$ and

$(\tau_{lon} + \tau_{lat}) \approx e_{SD.FS} = 17.6\%$ (Table 1). These figures represent lower-limit estimates, as $\tau_d = \rho g h \alpha_s$ (e.g. Van der Veen, 1999) should be larger for the high-order models, which hold thicker ice masses.

5.2 Response of the glacier to climate change

Before simulating the past and future dynamics of a glacier, it is useful to conduct a simple sensitivity test by imposing a step change in climate, i.e. mass balance, on the steady state geometry. This yields the characteristic timescales of a glacier, specifically the response times, which explain the length of time over which the glacier carries in its memory the mass balance history. On the corresponding steady state geometry of each model (Section 5.1), we impose $\Delta m(t) = \pm 1\,\mathrm{m}$ ice eq. a^{-1} in turn and we let the glacier respond until it attains a new steady state. The volume and length response of a glacier in each model case are plotted respectively in Figure 4c and 4d. Based on the e-folding concept (e.g. Jóhannesson et al., 1989), we calculate both the volume, t_v, and length response time, t_l, as the time required for a glacier to adjust $\left(1 - e^{-1}\right) \approx 63\%$ of total change in volume, ΔV, and length, ΔL, respectively.

Response times, t_v and t_l, are listed in Table 1; values are given for 2D flowline models as well. Based on these values, we note a few important points. First, a glacier takes less time, by ca. 17 (3D) and ca. 8 years (2D), to adjust its ice volume vs. its length. The relatively shorter t_v is primarily due to the instantaneous response of ice thickness to the climatic perturbation. Secondly, all models with a given spatial dimension yield nearly the same response times, i.e. $t_v \approx 25$ and $t_l \approx 42$ years (3D), and $t_v \approx 12$ and $t_l \approx 21$ years (2D). Leysinger Vieli & Gudmundsson (2004) find the same for 2D models, and they suggest that simpler models are sufficient for the purpose of estimating response times. This however does not imply that 2D models yield representative timescales for 3D cases. For the chosen geometry, 3D models appear to take twice as long to respond as the flowline models. This is mainly because the flowline models only capture the maximum velocity, along the central flowline, and hence adjust its geometry more quickly; whereas 3D models have an integrated ice flux across the glacier, which gives a slower average velocity, and consequently take longer time to adjust its geometry. Therefore, the flowline models, which lack the proper account of effects of varying glacier width, do not yield realistic estimates of response times for valley glaciers.

5.3 Projecting the glacier's future using flowline models

One of the key reasons for using dynamical ice flow models is to simulate the future states of a glacier under several possible climatic scenarios. To be able to obtain realistic predictions of ice volume, ice flow models should be constrained properly, ensuring that they truly represent the dynamics of the glacier at hand. Depending upon the availability of field data, this is usually accomplished through simulations of the ice surface velocities and/or historical front variations (e.g. Adhikari & Huybrechts, 2009). As we have considered synthetic glaciers, we take advantage to assume that the FS dynamics represents a real-world scenario and we constrain the reduced models accordingly. The majority of valley glacier simulations are based on flowline dynamics (e.g. Oerlemans et al., 1998); we choose PS2 and SIA2 models to reconstruct the past and project the future of a glacier.

By mimicking a real-world climatic history with inter-decadal variability, we impose a pre-defined $\Delta m(t)$ upon the FS model (Fig. 5a), and record the corresponding changes in the terminus position (Fig. 5b). For each of the PS2 and SIA2 models, we tune $\Delta m(t)$ so that

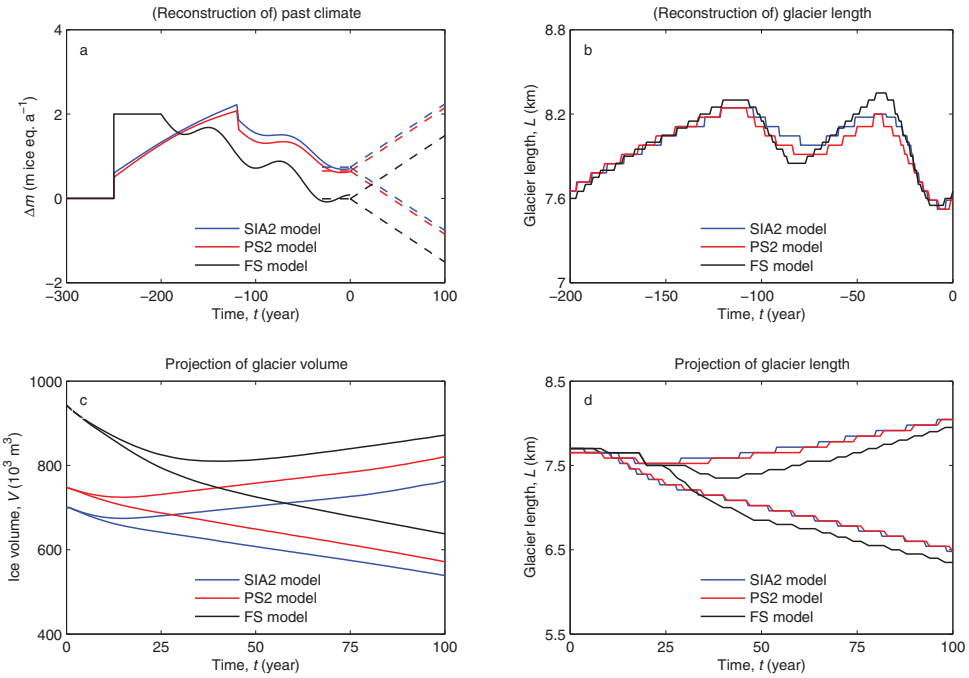

Fig. 5. Reconstructions of the past (a) climate and (b) glacier extent. A pre-defined $\Delta m(t)$ is imposed on the FS model to induce the evolution of glacier length. Using each of the PS2 and SIA2 models, the past $\Delta m(t)$ is then reconstructed so that the FS glacier extent is properly simulated. Future projections of (c) flowline ice volume and (d) glacier extent. Negative and positive times respectively indicate the past and future.

the model simulates such variations in the glacier length properly. The reconstructed glacier lengths and associated past climate are shown in Figure 5b and 5a, respectively. Due to the lack of high-order resistances, the PS2 and SIA2 models require a larger $\Delta m(t)$ in order to generate the (flowline) mass flux large enough to maintain the FS glacier lengths. With the corresponding climate history, the PS2 and SIA2 models are now ready to project the glacier's future.

With respect to the present climate, we consider two distinct scenarios for the future. The present climate is obtained by averaging the data of past 30 years. In addition to this, the future scenarios are defined as the linear changes in climate with $\Delta m(t) = \pm 1.5\,\mathrm{m}$ ice eq. a^{-1} by the end of $t = 100$ years (Fig. 5a). Under such climatic scenarios, we simulate each model to project the future dynamics of glacier. The evolutions of ice volume along the central flowline in a longitudinal band of unit width and glacier length are shown in Figures 5c and 5d, respectively. It is clear that the present time ($t = 0$ years) glacier lengths are similar in each model case; the corresponding ice volumes differ considerably, however. Short of tuning the ice dynamics (i.e. altering the ice viscosity or basal sliding rates), it is not possible to

constrain the reduced models to obtain both the FS length and volume at the same time. As discussed before (Section 5.1), the reduced models hold relatively smaller ice thickness and hence underestimate the ice volume, even if they yield the same glacier length. We could constrain the models so that they simulate the evolution of ice volume properly; in such cases the associated glacier lengths, however, would have been overestimated. This is not recommended, becasue ice volumes are unknown for most real-world glaciers.

Based on the reactions of ice volume and glacier length (Figs. 5c–5d), we note the following: (1) initially both the ice volume and glacier length decrease in each model case, even in the positive mass balance scenario, as a consequence of the generally decreasing trend of the past mass balance; (2) the times after which the glaciers start gaining ice volume and length (for the positive $\Delta m(t)$ scenario) are roughly equivalent to the corresponding values of t_v and t_l, respectively; (3) in the latter half of simulations, all models follow the similar trend for both the volume and length evolutions; (4) interestingly, the PS2 and SIA2 models slightly overestimate the glacier lengths, when they forecast lower ice volumes. The projected ice volumes and lengths after $t = 100$ years are summarized in Table 1. Due to its quick response to climate change and lack of resistances associated with high-order dynamics, the SIA2 model predicts reduced ice volumes, respectively by 6.4% and 14.0% on an average, than the PS2 and FS models. The reduced models, however, predict longer glaciers by 2.1%; this is probably because the FS model needs a longer time ($t_l = 42$ years, compared to flowline models, i.e. $t_l \approx 21$ years) to fully adjust the glacier length.

6. Summary and outlook

Based on the distinct physical mechanisms of land-based glacier dynamics, we present a simplified classification of models, namely the SD, PS and FS models. SD models are simplest and are based on the shallow-ice approximation, where local driving stress is solely balanced by the basal drag. The FS models, which solve a complete set of Stokes equations, are the most comprehensive. In addition to the basal drag, they also capture the effects of longitudinal stress gradients and lateral drag. The PS models, the intermediate complexity models, only deal with the basal drag and the longitudinal stress gradients. The main advantage of having these classes of models is that the scope of each model is clear. Since the dominant physical mechanisms in a given glaciological condition can easily be identified, one can choose the optimal model accordingly to yield realistic simulations. In the interior of the large ice sheets where the shallow-ice theory holds, for example, the computationally expedient SD models are optimal. For proper simulations of a narrow and steep valley glacier, however, FS models are essential, although they are numerically intensive.

We consider three different models, one from each model family, and compare them numerically at several stages of valley glacier modelling. Results are summarized in Table 1. We find that: (1) the high-order resistances are crucial to control the dynamics of gravity-driven ice flow, (2) absence of such resistances makes the reduced models yield larger velocities in diagnostic simulations and reduced ice thickness in prognostic simulations, (3) simpler flowline models, without accounting for the effects of varying glacier width, are not sufficient to yield realistic estimates of response times; they predict response times that are 50% too rapid to 3D models, and (4) constraining a model for the particular glacier application is not straightforward, as it is difficult to properly simulate the ice volume, glacier length and surface velocities altogether.

	FS model	PS model	SD model	$e_{PS.FS}$	$e_{SD.FS}$	$e_{SD.PS}$
	Steady state geometry and field variables					
Volume, V (10^6 m^3)	679.5	607.5	561.3	−10.6	−17.4	−7.6
Thickness, h (m)	133.0	119.4	111.8	−10.2	−15.9	−6.4
Velocity, u_x (m a^{-1})	69.2	80.8	85.5	16.7	23.6	5.9
Stress, τ_{xz} (kPa)	154.6	176.3	187.7	-	17.7	6.1
	Response timescales					
Timescale, t_v (a)	26.0	25.0	23.5	−3.8	−9.6	−6.0
$	-	12.5	12.0	−51.9	−53.8	-
Timescale, t_l (a)	42.0	42.0	41.0	0.0	−2.4	−2.4
$	-	21.5	20.5	−48.8	−51.2	-
	Future projections (after $t = 100$ years)					
Volume, V (10^3 m^3)*	871.8	821.1	762.9	−5.8	−12.5	−7.1
#	637.7	571.6	539.0	−10.4	−15.5	−5.7
Length, L (km)*	7.9	8.0	8.0	1.8	1.8	0.0
#	6.4	6.5	6.5	2.1	2.1	0.0

Table 1. Numerical comparison of several models, one from each model family. Errors between the models, e.g. $e_{PS.FS}$, are given in percentage. Response timescales are also calculated for flowline models ($). The future projection results represent for the central flowline; values are listed for both the positive (*) and negative (#) mass balance (Fig. 5a)

There are more than 200 k small glaciers and ice caps on Earth; it is not feasible to use the numerically intensive FS model to simulate every valley glacier. Therefore, we mostly encounter simple flowline models, e.g. the SIA2 and PS2 models, being used in the valley glacier applications. Without adding the numerical complexity, the dynamical reach of such models can be extended through the introduction of parameterized correction factors. The effects of longitudinal stress gradients can be accounted for by embedding L-factors (Adhikari & Marshall, 2011); the lateral drag associated with the valley walls (Nye, 1965) and stick/slip basal interface (Adhikari & Marshall, in preperation) can also be captured via analogous correction factors. This offers a pragmatic middle ground for simulating glacier response to climate change.

Undoubtedly, the biggest challenge in glacier modelling is the lack of sufficient field data. Geometric and climatic data (e.g. basal and surface topographies, glacier length records, and mass balance fields), as well as observations of ice velocities, are not available in most cases. They are essential to justify the cost of using complex, 3D, FS models. Furthermore, the lack of proper theories and associated data to describe basal processes, e.g. basal sliding, is also a subject of concern that we have not discussed in the text; in many cases, poor characterization of basal flow is the limiting factor in modelling glacier dynamics.

7. Acknowledgements

We acknowledge support from the Western Canadian Cryospheric Network (WC^{2}N), funded by the Canadian Foundation for Climate and Atmospheric Sciences (CFCAS), and the Natural Sciences and Engineering Research Council (NSERC) of Canada.

8. Appendix

Appendix A: Diagnostic equations

We present the governing equations, with field variables u and p, for each model introduced in Section 3.1. The continuity equation (Eq. 5) holds in all cases; it takes the following respective form for 3D and 2D (flowline) models,

$$\frac{\partial u_x}{\partial x} + \frac{\partial u_y}{\partial y} + \frac{\partial u_z}{\partial z} = 0, \tag{A1}$$

$$\frac{\partial u_x}{\partial x} + \frac{\partial u_z}{\partial z} = 0. \tag{A2}$$

Hereafter, the velocity components, $\{u_x \;\; u_y \;\; u_z\}^T$, are simply denoted by $\{u \;\; v \;\; w\}^T$.

The differences between the models arise from the approximations made in the momentum balance equation itself (Eq. 6) and in the definition of strain-rate tensor (Eq. 4). Assuming that g_z (hereafter denoted by g) is the only non-zero component of gravity vector, we obtain the governing equations associated with the momentum balance via Equations (7) and (1–4). The algebraic process is straightforward; we simply quote the results for each model.

A1: The FS model

This full-system 3D model has no such approximations at all. Along with Equation (A1), followings are the governing equations for the FS model,

$$2\frac{\partial}{\partial x}\left(\eta\frac{\partial u}{\partial x}\right) + \frac{\partial}{\partial y}\left(\eta\frac{\partial u}{\partial y}\right) + \frac{\partial}{\partial z}\left(\eta\frac{\partial u}{\partial z}\right) + \frac{\partial}{\partial y}\left(\eta\frac{\partial v}{\partial x}\right) + \frac{\partial}{\partial z}\left(\eta\frac{\partial w}{\partial x}\right) + \frac{\partial p}{\partial x} = 0, \tag{A3}$$

$$\frac{\partial}{\partial x}\left(\eta\frac{\partial u}{\partial y}\right) + \frac{\partial}{\partial x}\left(\eta\frac{\partial v}{\partial x}\right) + 2\frac{\partial}{\partial y}\left(\eta\frac{\partial v}{\partial y}\right) + \frac{\partial}{\partial z}\left(\eta\frac{\partial v}{\partial z}\right) + \frac{\partial}{\partial z}\left(\eta\frac{\partial w}{\partial y}\right) + \frac{\partial p}{\partial y} = 0, \tag{A4}$$

$$\frac{\partial}{\partial x}\left(\eta\frac{\partial u}{\partial z}\right) + \frac{\partial}{\partial y}\left(\eta\frac{\partial v}{\partial z}\right) + \frac{\partial}{\partial x}\left(\eta\frac{\partial w}{\partial x}\right) + \frac{\partial}{\partial y}\left(\eta\frac{\partial w}{\partial y}\right) + 2\frac{\partial}{\partial z}\left(\eta\frac{\partial w}{\partial z}\right) + \frac{\partial p}{\partial z} + \rho g = 0, \tag{A5}$$

where the nonlinear effective viscosity, η, is given by Equation (2) with

$$2\dot{\epsilon}_e^2 = \frac{\partial^2 u}{\partial x^2} + \frac{\partial^2 v}{\partial y^2} + \frac{\partial^2 w}{\partial z^2} + \frac{1}{2}\left[\left(\frac{\partial u}{\partial y} + \frac{\partial v}{\partial x}\right)^2 + \left(\frac{\partial v}{\partial z} + \frac{\partial w}{\partial y}\right)^2 + \left(\frac{\partial w}{\partial x} + \frac{\partial u}{\partial z}\right)^2\right]. \tag{A6}$$

A2: The PS model

In this family of models, we make two approximations to ensure that the effects of lateral drag are completely absent. We neglect (1) the lateral variation of stress deviators, i.e. $\tau_{ij,y} = 0$, and (2) reduce the definition of $\dot{\epsilon}$ by excluding the lateral variation of ice velocities, i.e. $u_{i,y} = 0$. Along with Equation (A1), the **PS3 model** has the following governing equations,

$$2\frac{\partial}{\partial x}\left(\eta\frac{\partial u}{\partial x}\right) + \frac{\partial}{\partial z}\left(\eta\frac{\partial u}{\partial z}\right) + \frac{\partial}{\partial z}\left(\eta\frac{\partial w}{\partial x}\right) + \frac{\partial p}{\partial x} = 0, \tag{A7}$$

$$\frac{\partial}{\partial x}\left(\eta\frac{\partial v}{\partial x}\right) + \frac{\partial}{\partial z}\left(\eta\frac{\partial v}{\partial z}\right) + \frac{\partial p}{\partial y} = 0, \tag{A8}$$

$$\frac{\partial}{\partial x}\left(\eta\frac{\partial u}{\partial z}\right)+\frac{\partial}{\partial x}\left(\eta\frac{\partial w}{\partial x}\right)+2\frac{\partial}{\partial z}\left(\eta\frac{\partial w}{\partial z}\right)+\frac{\partial p}{\partial z}+\rho g=0, \tag{A9}$$

where the nonlinear effective viscosity, η, is given by Equation (2) with

$$2\dot{\epsilon}_e^2=\frac{\partial^2 u}{\partial x^2}+\frac{\partial^2 w}{\partial z^2}+\frac{1}{2}\left[\frac{\partial^2 v}{\partial x^2}+\frac{\partial^2 v}{\partial z^2}+\left(\frac{\partial w}{\partial x}+\frac{\partial u}{\partial z}\right)^2\right]. \tag{A10}$$

The **PS2 model** is a 2D Stokes model, strictly following the plane-strain approximations (after neglecting the non-zero τ_{yy}, which is required to maintain $\dot{\epsilon}_{yy}=0$). Equations (A2), (A7) and (A9) form the governing equations, where η is given by Equation (2) with

$$2\dot{\epsilon}_e^2=\frac{\partial^2 u}{\partial x^2}+\frac{\partial^2 w}{\partial z^2}+\frac{1}{2}\left(\frac{\partial w}{\partial x}+\frac{\partial u}{\partial z}\right)^2. \tag{A11}$$

A3: The SD model

This family of models does not account for the effects of longitudinal stress gradients, as well as those of lateral drag. Consequently, the vertical shear stresses are the only non-zero stress components. In addition, the reduced definition of $\dot{\epsilon}$ approximated in the PS models is also applied here. Along with Equation (A1), the governing equations for the **SD3 model** are,

$$\frac{\partial}{\partial z}\left(\eta\frac{\partial u}{\partial z}\right)+\frac{\partial}{\partial z}\left(\eta\frac{\partial w}{\partial x}\right)+\frac{\partial p}{\partial x}=0, \tag{A12}$$

$$\frac{\partial}{\partial z}\left(\eta\frac{\partial v}{\partial z}\right)+\frac{\partial p}{\partial y}=0, \tag{A13}$$

$$\frac{\partial}{\partial x}\left(\eta\frac{\partial u}{\partial z}\right)+\frac{\partial}{\partial x}\left(\eta\frac{\partial w}{\partial x}\right)+\frac{\partial p}{\partial z}+\rho g=0, \tag{A14}$$

where the nonlinear effective viscosity, η, is given by Equation (2) with

$$2\dot{\epsilon}_e^2=\frac{1}{2}\left[\frac{\partial^2 v}{\partial z^2}+\left(\frac{\partial w}{\partial x}+\frac{\partial u}{\partial z}\right)^2\right]. \tag{A15}$$

Equations (A2), (A12) and (A14) are the governing equations for the **SD2 model**, where η is given by Equation (2) with

$$2\dot{\epsilon}_e^2=\frac{1}{2}\left(\frac{\partial w}{\partial x}+\frac{\partial u}{\partial z}\right)^2. \tag{A16}$$

Further approximations are needed to obtain the standard SIA models; (1) the horizontal gradients in stresses are negligible, i.e. $\tau_{ij,x}=0$, and (2) the definition of $\dot{\epsilon}$ is further reduced by excluding the horizontal gradients of velocities, i.e. $u_{i,x}=0$. Hence, in addition to Equation (A1), the **SIA3 model** has the following governing equations,

$$\frac{\partial}{\partial z}\left(\eta\frac{\partial u}{\partial z}\right)+\frac{\partial p}{\partial x}=0, \tag{A17}$$

$$\frac{\partial}{\partial z}\left(\eta\frac{\partial v}{\partial z}\right)+\frac{\partial p}{\partial y}=0, \tag{A18}$$

$$\frac{\partial p}{\partial z} + \rho g = 0, \tag{A19}$$

where the nonlinear effective viscosity, η, is given by Equation (2) with

$$2\dot{\epsilon}_e^2 = \frac{1}{2}\left(\frac{\partial^2 v}{\partial z^2} + \frac{\partial^2 u}{\partial z^2}\right). \tag{A20}$$

The set of Equations (A2), (A17) and (A19) form the governing equations for the **SIA2 model**, where η is given by Equation (2) with

$$2\dot{\epsilon}_e^2 = \frac{1}{2}\frac{\partial^2 u}{\partial z^2}. \tag{A21}$$

With a simple algebraic manipulation of the governing equations for SIA2 model, one can obtain the analytical solution for $u(x,z)$ in a laminar flow (Eq. 8). The corresponding solution for $w(x,z)$ follows directly from the incompressibility criterion (Eq. A2).

Appendix B: FE formulation of diagnostic equations

Here, we construct a linear system of Equations (12) and (13) for the FS model; those for the reduced models can be obtained in a similar manner. The LHSs of governing equations (Eqs. A3–A5 and A1), after imposing the approximations of field variables, represent the system residuals, i.e. the terms inside the large parentheses in Equations (12–13). So, expanding Equation (13) in horizontal x axis, for example, gives

$$\int_{\Omega_e} \psi_i \left[2\frac{\partial\left(\eta\frac{\partial\tilde{u}}{\partial x}\right)}{\partial x} + \frac{\partial\left(\eta\frac{\partial\tilde{u}}{\partial y}\right)}{\partial y} + \frac{\partial\left(\eta\frac{\partial\tilde{u}}{\partial z}\right)}{\partial z} + \frac{\partial\left(\eta\frac{\partial\tilde{v}}{\partial x}\right)}{\partial y} + \frac{\partial\left(\eta\frac{\partial\tilde{w}}{\partial x}\right)}{\partial z} + \frac{\partial\tilde{p}}{\partial x} \right] \mathrm{d}\Omega_e = 0. \tag{B1}$$

Similar equations can be obtained for the second horizontal and vertical directions, and also for the incompressibility criterion (Eq. 12).

Applying Green-Gauss theorem to integrate Equation (B1) by parts (Rao, 2005), we obtain,

$$\begin{aligned}
&-\int_{\Omega_e} 2\frac{\partial\psi_i}{\partial x}\left(\eta\frac{\partial\tilde{u}}{\partial x}\right)\mathrm{d}x\mathrm{d}y\mathrm{d}z + \int_{\Gamma_e} 2\psi_i\left(\eta\frac{\partial\tilde{u}}{\partial x}\right)n_x\,\mathrm{d}S - \int_{\Omega_e}\frac{\partial\psi_i}{\partial y}\left(\eta\frac{\partial\tilde{u}}{\partial y}\right)\mathrm{d}x\mathrm{d}y\mathrm{d}z + \\
&\quad + \int_{\Gamma_e}\psi_i\left(\eta\frac{\partial\tilde{u}}{\partial y}\right)n_y\,\mathrm{d}S - \int_{\Omega_e}\frac{\partial\psi_i}{\partial z}\left(\eta\frac{\partial\tilde{u}}{\partial z}\right)\mathrm{d}x\mathrm{d}y\mathrm{d}z + \int_{\Gamma_e}\psi_i\left(\eta\frac{\partial\tilde{u}}{\partial z}\right)n_z\,\mathrm{d}S + \\
&-\int_{\Omega_e}\frac{\partial\psi_i}{\partial y}\left(\eta\frac{\partial\tilde{v}}{\partial x}\right)\mathrm{d}x\mathrm{d}y\mathrm{d}z + \int_{\Gamma_e}\psi_i\left(\eta\frac{\partial\tilde{v}}{\partial x}\right)n_y\,\mathrm{d}S - \int_{\Omega_e}\frac{\partial\psi_i}{\partial z}\left(\eta\frac{\partial\tilde{w}}{\partial x}\right)\mathrm{d}x\mathrm{d}y\mathrm{d}z + \\
&\quad + \int_{\Gamma_e}\psi_i\left(\eta\frac{\partial\tilde{w}}{\partial x}\right)n_z\,\mathrm{d}S - \int_{\Omega_e}\frac{\partial\psi_i}{\partial x}\tilde{p}\,\mathrm{d}x\mathrm{d}y\mathrm{d}z + \int_{\Gamma_e}\psi_i\tilde{p}n_x\,\mathrm{d}S = 0,
\end{aligned} \tag{B2}$$

where $\mathrm{d}S \in \Gamma_e$ is a boundary surface, and $\{n_x \;\; n_y \;\; n_z\}^T$ are the x, y and z components of the unit normal at the boundary surface.

By substituting approximations of field variables (Eqs. 10–11) into Equation (B2), we obtain

$$\int_{\Omega_e} \eta \left(2\frac{\partial \psi_i}{\partial x}\frac{\partial [\psi]}{\partial x} + \frac{\partial \psi_i}{\partial y}\frac{\partial [\psi]}{\partial y} + \frac{\partial \psi_i}{\partial z}\frac{\partial [\psi]}{\partial z} \right) \{u\}\, \mathrm{d}x\mathrm{d}y\mathrm{d}z + \int_{\Omega_e} \eta \frac{\partial \psi_i}{\partial y}\frac{\partial [\psi]}{\partial x} \{v\}\, \mathrm{d}x\mathrm{d}y\mathrm{d}z + \int_{\Omega_e} \eta \frac{\partial \psi_i}{\partial z}\frac{\partial [\psi]}{\partial x} \{w\}\, \mathrm{d}x\mathrm{d}y\mathrm{d}z + \int_{\Omega_e} \frac{\partial \psi_i}{\partial x} [\psi] \{p\}\, \mathrm{d}x\mathrm{d}y\mathrm{d}z = \int_{\Gamma_e} \psi_i \left[\left(2\eta \frac{\partial \tilde{u}}{\partial x} + \tilde{p} \right) n_x + \eta \left(\frac{\partial \tilde{u}}{\partial y} + \frac{\partial \tilde{v}}{\partial x} \right) n_y + \eta \left(\frac{\partial \tilde{u}}{\partial z} + \frac{\partial \tilde{w}}{\partial x} \right) n_z \right] \mathrm{d}S. \tag{B3}$$

Here, the RHS surface integral forms a Neumann or natural boundary condition. With Equations (4), (1), and (7), the terms inside large parentheses take the following forms,

$$\left(2\eta \frac{\partial \tilde{u}}{\partial x} + \tilde{p} \right) n_x + \eta \left(\frac{\partial \tilde{u}}{\partial y} + \frac{\partial \tilde{v}}{\partial x} \right) n_y + \eta \left(\frac{\partial \tilde{u}}{\partial z} + \frac{\partial \tilde{w}}{\partial x} \right) n_z = \sigma_{xx} n_x + \sigma_{xy} n_y + \sigma_{xz} n_z. \tag{B4}$$

The RHS term above indicates the horizontal x component of the Cauchy stress tensor on the boundary surface. Denoting this by σ_x, we rewrite Equation (B3) as,

$$\int_{\Omega_e} \eta \left(2\frac{\partial \psi_i}{\partial x}\frac{\partial [\psi]}{\partial x} + \frac{\partial \psi_i}{\partial y}\frac{\partial [\psi]}{\partial y} + \frac{\partial \psi_i}{\partial z}\frac{\partial [\psi]}{\partial z} \right) \{u\}\, \mathrm{d}x\mathrm{d}y\mathrm{d}z + \int_{\Omega_e} \eta \frac{\partial \psi_i}{\partial y}\frac{\partial [\psi]}{\partial x} \{v\}\, \mathrm{d}x\mathrm{d}y\mathrm{d}z + \int_{\Omega_e} \eta \frac{\partial \psi_i}{\partial z}\frac{\partial [\psi]}{\partial x} \{w\}\, \mathrm{d}x\mathrm{d}y\mathrm{d}z + \int_{\Omega_e} \frac{\partial \psi_i}{\partial x} [\psi] \{p\}\, \mathrm{d}x\mathrm{d}y\mathrm{d}z = \int_{\Gamma_e} \psi_i \sigma_x\, \mathrm{d}S. \tag{B5}$$

Similar equations can be written, respectively for horizontal y and vertical z directions,

$$\int_{\Omega_e} \eta \frac{\partial \psi_i}{\partial x}\frac{\partial [\psi]}{\partial y} \{u\}\, \mathrm{d}x\mathrm{d}y\mathrm{d}z + \int_{\Omega_e} \eta \left(\frac{\partial \psi_i}{\partial x}\frac{\partial [\psi]}{\partial x} + 2\frac{\partial \psi_i}{\partial y}\frac{\partial [\psi]}{\partial y} + \frac{\partial \psi_i}{\partial z}\frac{\partial [\psi]}{\partial z} \right) \{v\}\, \mathrm{d}x\mathrm{d}y\mathrm{d}z + \int_{\Omega_e} \eta \frac{\partial \psi_i}{\partial z}\frac{\partial [\psi]}{\partial y} \{w\}\, \mathrm{d}x\mathrm{d}y\mathrm{d}z + \int_{\Omega_e} \frac{\partial \psi_i}{\partial y} [\psi] \{p\}\, \mathrm{d}x\mathrm{d}y\mathrm{d}z = \int_{\Gamma_e} \psi_i \sigma_y\, \mathrm{d}S, \tag{B6}$$

$$\int_{\Omega_e} \eta \frac{\partial \psi_i}{\partial x}\frac{\partial [\psi]}{\partial z} \{u\}\, \mathrm{d}x\mathrm{d}y\mathrm{d}z + \int_{\Omega_e} \eta \frac{\partial \psi_i}{\partial y}\frac{\partial [\psi]}{\partial z} \{v\}\, \mathrm{d}x\mathrm{d}y\mathrm{d}z + \int_{\Omega_e} \eta \left(\frac{\partial \psi_i}{\partial x}\frac{\partial [\psi]}{\partial x} + \frac{\partial \psi_i}{\partial y}\frac{\partial [\psi]}{\partial y} + 2\frac{\partial \psi_i}{\partial z}\frac{\partial [\psi]}{\partial z} \right) \{w\}\, \mathrm{d}x\mathrm{d}y\mathrm{d}z + \int_{\Omega_e} \frac{\partial \psi_i}{\partial z} [\psi] \{p\}\, \mathrm{d}x\mathrm{d}y\mathrm{d}z = \int_{\Omega_e} \rho g \psi_i\, \mathrm{d}x\mathrm{d}y\mathrm{d}z + \int_{\Gamma_e} \psi_i \sigma_z\, \mathrm{d}S, \tag{B7}$$

where $\sigma_y \left(= \sigma_{xy} n_x + \sigma_{yy} n_y + \sigma_{yz} n_z \right)$ and $\sigma_z \left(= \sigma_{xz} n_x + \sigma_{yz} n_y + \sigma_{zz} n_z \right)$ are y and z components of σ on the boundary surface, respectively. For the stress free boundary condition, the surface integrals in Equations (B5–B7) become zeros.

The incompressibility criterion (Eq. 12) can simply be expanded as,

$$\int_{\Omega_e} \psi_i \frac{\partial [\psi]}{\partial x} \{u\}\, \mathrm{d}x\mathrm{d}y\mathrm{d}z + \int_{\Omega_e} \psi_i \frac{\partial [\psi]}{\partial y} \{v\}\, \mathrm{d}x\mathrm{d}y\mathrm{d}z + \int_{\Omega_e} \psi_i \frac{\partial [\psi]}{\partial z} \{w\}\, \mathrm{d}x\mathrm{d}y\mathrm{d}z = 0. \tag{B8}$$

Now, we write the linear equations (Eqs. B5–B8) in the following elemental matrix form,

$$[K] \{\phi\} = \{F\}, \tag{B9}$$

where $[K]$ is the coefficient matrix, $\{\phi\}$ is comprised of unknown field variables, and $\{F\}$ is the RHS force vector. They are given by,

$$\begin{bmatrix} [K_*^{11}] & [K^{12}] & [K^{13}] & [K^{10}] \\ [K^{21}] & [K_*^{22}] & [K^{23}] & [K^{20}] \\ [K^{31}] & [K^{32}] & [K_*^{33}] & [K^{30}] \\ [K^{10}]^T & [K^{20}]^T & [K^{30}]^T & [0] \end{bmatrix} \begin{Bmatrix} \{u\} \\ \{v\} \\ \{w\} \\ \{p\} \end{Bmatrix} = \begin{Bmatrix} \{F^1\} \\ \{F^2\} \\ \{F^3\} \\ \{0\} \end{Bmatrix}, \tag{B10}$$

Components of the coefficient matrix and the force vector are as follow,

$$[K_*^{\alpha\alpha}] = [K^{\alpha\alpha}] + \left[K^{11}\right] + \left[K^{22}\right] + \left[K^{33}\right];\ \alpha = 1,2,3, \tag{B11}$$

$$K_{ij}^{\alpha\beta} = \int_{\Omega_e} \eta \frac{\partial \psi_i}{\partial \chi_\beta} \frac{\partial \psi_j}{\partial \chi_\alpha}\, \mathrm{d}x\mathrm{d}y\mathrm{d}z;\ \alpha,\beta = 1,2,3, \tag{B12}$$

$$K_{ij}^{\alpha 0} = \int_{\Omega_e} \eta \frac{\partial \psi_i}{\partial \chi_\alpha} \psi_j\, \mathrm{d}x\mathrm{d}y\mathrm{d}z;\ \alpha = 1,2,3, \tag{B13}$$

$$F^\alpha = \int_{\Gamma_e} \psi_i \sigma_\alpha\, \mathrm{d}S;\ \alpha = 1,2, \tag{B14}$$

$$F^3 = \int_{\Omega_e} \rho g \psi_i\, \mathrm{d}x\mathrm{d}y\mathrm{d}z + \int_{\Gamma_e} \psi_i \sigma_z\, \mathrm{d}S, \tag{B15}$$

where χ denotes the Cartesian coordinates with subscripts $(1,2,3)$ for (x,y,z). Similarly, (σ_1,σ_2) in Equation (B14) denote (σ_x,σ_y), respectively.

Now, we assemble the elemental equation (Eq. B9) to get the global equation,

$$[\mathbf{K}]\{\mathbf{\Phi}\} = \{\mathbf{F}\}, \tag{B16}$$

where $[\mathbf{K}] = \sum_{e=1}^{E}[K]$, $\{\mathbf{\Phi}\} = \sum_{e=1}^{E}\{\phi\}$, $\{\mathbf{F}\} = \sum_{e=1}^{E}\{F\}$, and E is the total number of elements e within the global domain Ω.

Appendix C: Diagnostic system stabilization

We use superscript of *stb* to refer to the stabilization contributions to the elemental matrices and vectors. With stabilization terms, Equation (B9) takes the following form

$$\left[[K] + \left[K^{stb}\right]\right]\{\phi\} = \left\{\{F\} + \left\{F^{stb}\right\}\right\}. \tag{C1}$$

For the FS model, the residual matrix, $[R_\sigma]$, associated with the momentum balance equation (see Eq. 14) can be obtained from Equations (A3–A5),

$$[R_\sigma] = \begin{bmatrix} [R_*^{11}] & [R^{12}] & [R^{13}] & [R^{10}] \\ [R^{21}] & [R_*^{22}] & [R^{23}] & [R^{20}] \\ [R^{31}] & [R^{32}] & [R_*^{33}] & [R^{30}] \\ [0] & [0] & [0] & [0] \end{bmatrix}, \tag{C2}$$

where

$$[R_*^{\alpha\alpha}] = [R^{\alpha\alpha}] + \left[R^{11}\right] + \left[R^{22}\right] + \left[R^{33}\right];\ \alpha = 1,2,3, \tag{C3}$$

$$R_i^{\alpha\beta} = \frac{\partial}{\partial \chi_\beta}\left(\eta \frac{\partial \psi_i}{\partial \chi_\alpha}\right);\ \alpha, \beta = 1, 2, 3, \tag{C4}$$

$$R_i^{\alpha 0} = \frac{\partial \psi_i}{\partial \chi_\alpha};\ \alpha = 1, 2, 3, \tag{C5}$$

Similarly, the corresponding residual matrix, $[R_u]$, associated with the continuity equation is obtained from Equation (A1),

$$[R_u] = \left[\begin{array}{cccc} \frac{\partial \psi_i}{\partial x} & \frac{\partial \psi_i}{\partial y} & \frac{\partial \psi_i}{\partial z} & [0] \end{array}\right]. \tag{C6}$$

Referring to Equations (14–15), the stabilization contributions to the elemental matrix and the RHS force vector take the following respective forms,

$$\left[K^{stb}\right] = \delta_1 \left[R_\sigma\right]^T \left[R_\sigma\right] + \delta_2 \left[R_u\right]^T \left[R_u\right], \tag{C7}$$

$$\left[F^{stb}\right] = \delta_1 \left[F\right]^T \left[R_\sigma\right], \tag{C8}$$

where $[F]$ is the force vector, given in the RHS of Equation (B10).

Appendix D: FE formulation and stabilization of prognostic equations

Equation (18), in a three-dimensional space, can be expanded as,

$$\int_{\Gamma_e} \psi_i^s \left[\frac{\partial \tilde{s}}{\partial t} + u\frac{\partial \tilde{s}}{\partial x} + v\frac{\partial \tilde{s}}{\partial y} - (w + m)\right] \mathrm{d}\Gamma_e = 0. \tag{D1}$$

With approximation of field variable (Eq. 17), Equation (D1) becomes,

$$\int_{\Gamma_e} \psi_i \left[\psi\right] \frac{\partial \left\{s\right\}}{\partial t}\, \mathrm{d}S + \int_{\Gamma_e} \psi_i \left(u\frac{\partial \left[\psi\right]}{\partial x} + v\frac{\partial \left[\psi\right]}{\partial y}\right) \left\{s\right\} \mathrm{d}S = \int_{\Gamma_e} \psi_i \left(w + m\right) \mathrm{d}S, \tag{D2}$$

which can be expressed in the following elemental matrix form,

$$\left[\left[M\right] + \left[M^{stb}\right]\right] \frac{\partial \left\{\phi\right\}}{\partial t} + \left[\left[K\right] + \left[K^{stb}\right]\right] \left\{\phi\right\} = \left\{\left\{F\right\} + \left\{F^{stb}\right\}\right\}, \tag{D3}$$

where

$$\left[M\right] = \left[\int_{\Gamma_e} \psi_i \psi_j \, \mathrm{d}S\right], \ \left[M^{stb}\right] = \left\langle \psi_i, \delta_3 R_s \right\rangle, \tag{D4}$$

$$\left[K\right] = \left[\int_{\Gamma_e} \psi_i \left(u\frac{\partial \psi_j}{\partial x} + v\frac{\partial \psi_j}{\partial y}\right) \mathrm{d}S\right], \ \left[K^{stb}\right] = \left\langle R_s, \delta_3 R_s \right\rangle, \tag{D5}$$

$$\left\{F\right\} = \left\{\int_{\Gamma_e} \psi_i \left(w + m\right) \mathrm{d}S\right\}, \ \left\{F^{stb}\right\} = \left\langle \left(w + m\right), \delta_3 R_s \right\rangle, \tag{D6}$$

$$\left[R_s\right] = \left[u\frac{\partial \psi_i}{\partial x} + v\frac{\partial \psi_i}{\partial y}\right], \tag{D7}$$

Here, δ_3 is the stability parameter that is a function of element size, h_k, and the norm of velocity vector, such that $\delta_3 = \frac{h_k}{2\|u\|}$. The mass matrix, $[M]$, deals with the evolution of glacier surface. Matrices and vectors with superscript *stb* are once again the stabilization contributions. The elemental equation (Eq. D3) can be assembled into the global matrix, as for Equation (B9).

9. References

Adhikari, S. & Huybrechts, P. (2009). Numerical modelling of historical front variations and the 21st-century evolution of glacier AX010, Nepal Himalaya, *Ann. Glaciol.* 50(52): 27–34.

Adhikari, S. & Marshall, S. (2011). Improvements to shear-deformational models of glacier dynamics through a longitudinal stress factor, *J. Glaciol.* 57(206): 1003–1016.

Adhikari, S. & Marshall, S. (in preperation). Parameterization of slip-induced lateral drag in flowline models of glacier dynamics.

Allen, S., Schneider, D. & Owens, I. (2009). First approaches towards modelling glacial hazards in the Mount Cook region of New Zealand's Southern Alps, *Nat. Hazard Earth Sys.* 9(2): 481–499.

Alley, R. (1992). Flow-law hypotheses for ice-sheet modeling, *J. Glaciol.* 38(129): 245–256.

Bamber, J., Layberry, R. & Gogineni, S. (2001). A new ice thickness and bed data set for the greenland ice sheet, 1. Measurement, data reduction, and errors, *J. Geophys. Res.* 106: 33733–33780.

Baral, D., Hutter, K. & Greve, R. (2001). Asymptotic theories of large-scale motion, temperature, and moisture distribution in land-based polythermal ice sheets: a critical review and new developments, *Appl. Mech. Rev.* 54: 215–256.

Beedle, M., Menounos, B., Luckman, B. & Wheate, R. (2009). Annual push moraines as climate proxy, *Geophys. Res. Lett.* 36: L20501.

Blatter, H. (1995). Velocity and stress fields in grounded glaciers: a simple algorithm for including deviatoric stress gradients, *J. Glaciol.* 41(138): 333–344.

Blatter, H., Greve, R. & Abe-Ouchi, A. (2010). A short history of the thermomechanical theory and modelling of glaciers and ice sheets, *J. Glaciol.* 56(200): 1087–1094.

Budd, W. & Jacka, T. (1989). A review of ice rheology for ice sheet modelling, *Cold Re. Sci. Technol.* 16: 107–144.

Budd, W. & Jenssen, D. (1975). Numerical modelling of glacier systems, *IASH Publ.* 104: 257–291.

Bueler, E., Brown, J. & Lingle, C. (2007). Exact solutions to the thermomechanically coupled shallow-ice approximation: effective tools for varification, *J. Glaciol.* 53(182): 499–516.

Calov, R. & Hutter, K. (1996). Thermo mechanical response of the Greenland ice sheet to various climate scenarios, *Clim. Dynam.* 12(4): 243–260.

Campbell, W. & Rasmussen, L. (1969). Three-dimensional surges and recoveries in a numerical glacier model, *J. Glaciol.* 6(4): 979–986.

Chow, S., Carey, G. & Anderson, M. (2004). Finite element approximations of a glaciological problem, *ESAIM-Math. Model Num.* 38(5): 741–756.

Christensen, J., Hewitson, B., Busuioc, A., Chen, A., Gao, X., Held, I., Jones, R., Kolli, R., Kwon, W.-T., Laprise, R., Magaña Rueda, V., Mearns, L., Menéndez, C., Räisänen, J., Rinke, A., Sarr, A. & Whetton, P. (2007). Regional climate projections, *in* S. Solomon & 7 others (eds), *Climate Change 2007: The Physical Science Basis. Contribution of WG I to the Fourth Assessment Report of the IPCC*, Cambridge Univ. Press, Cambridge, pp. 847–940.

Clarke, G. (1987). A short history of scientific investigations on glaciers, *J. Glaciol.* Special Issue: 4–24.

Colinge, J. & Blatter, H. (1998). Stress and velocity fields in glaciers: Part I. Finite-difference schemes for higher-order glacier models, *J. Glaciol.* 44: 448–456.

Colinge, J. & Rappaz, J. (1999). A strongly nonlinear problem arising in glaciology, *ESAIM-Math. Model Num.* 33(2): 395–406.

Cook, A. J., Fox, A. J., Vaughan, D. G. & Ferrigno, J. G. (2005). Retreating glacier fronts on the antarctic peninsula over the past half-century, *Science* 308(5721): 541–544.

Cuffey, K. & Paterson, W. (2010). *The Physics of Glaciers*, fourth edn, Butterworth Heinemann, Elsevier.

Donea, J. & Huerta, A. (2003). *Finite Element Methods for Flow Problems*, John Wiley and Sons.

Dyurgerov, M. & Meier, M. (2005). *Glaciers and the Changing Earth System: A 2004 snapshot*, Occasional paper 58, Institute of Arctic and Alpine Research, U. Colorado, Boulder.

Franca, L. & Frey, S. (1992). Stabilized finite element methods: II the incompressibility Navier-Stokes equations, *Comput. Method Appl. M.* 99: 209–233.

Gagliardini, O. & Zwinger, T. (2008). The ISMIP-HOM benchmark experiments performed using the Finite-Element code Elmer, *The Cryosphere* 2(1): 67–76.

Gillet-Chaulet, F., Gagliardini, O., Meyssonnier, J., Montagnat, M. & Castelnau, O. (2005). A user-friendly anisotropic fow law for ice-sheet modelling, *J. Glaciol.* 51(172): 3–14.

Gillett, N., Arora, V., Zickfeld, K., Marshall, S. & Merryfield, W. (2011). Ongoing climate change following a complete cessation of carbon dioxide emissions, *Nature Geosci.* 4: 83–87.

Glen, J. (1952). Experiments on the deformation of ice, *J. Glaciol.* 2(12): 111–114.

Glen, J. (1955). The creep of polycrystalline ice, *Proc. R. Soc. London, Ser. A* 228: 519–538.

Glen, J. (1958). The flow law of ice: a discussion of the assumptions made in glacier theory, their experimental foundations and consequences, *Int. Assoc. Hydrol. Sci. Pub.* 47: 171–183.

Glowinski, R. & Rappaz, J. (2003). Approximation of a nonlinear elliptic problem arising in a non-Newtonian fluid flow model in glaciology, *ESAIM-Math. Model Num.* 37(1): 175–186.

Goelzer, H., Huybrechts, P., Loutre, M., Goosse, H., Fichefet, T. & Mouchet, A. (2011). Impact of Greenland and Antarctic ice sheet interactions on climate sensitivity, *Clim. Dynam.* 37: 1005–1018.

Gudmundsson, G. (1999). A three-dimensional numerical model of the confluence area of Unteraargletscher, Bernese Alps, Switzerland, *J. Glaciol.* 45(150): 219–230.

Hanson, B. (1995). A fully three-dimensional finite-element model applied to velocities on Storglaciaren, Sweden, *J. Glaciol.* 41 (137): 91–102.

Hindmarsh, R. (2004). A numerical comparison of approximations to the stokes-equations used in the ice sheet and glacier modeling, *J. Geophys. Res.* 109: F01012.

Hoffman, P. & Schrag, D. (2000). Snowball earth, *Sci. Am.* 282: 62–75.

Hood, P. & Taylor, C. (1974). Navier-Stokes equations using mixed interpolation, *in* J. Oden, O. Zienkiewicz, R. Gallagher & C. Taylor (eds), *Finite Element Methods in Flow Problems*, UAH Press, pp. 121–132.

Hooke, R. (1981). Flow law for polycrystalline ice in glaciers: comparison of theoretical predictions, laboratory data and field measurements, *Rev. Geophys. Space Phys.* 19: 664–672.

Hutter, K. (1983). *Theoretical Glaciology: Material Science of Ice and the Mechanics of Glaciers and Ice Sheets*, Reidel, Dordrecht, Netherlands.

Huybrechts, P., Goelzer, H., Janssens, I., Driesschaert, E., Fichefet, T., Goosse, H. & Loutre, M. (2011). Response of the Greenland and Antarctic ice sheets to multi-millennial greenhouse warming in the Earth system model of intermediate complexity LOVECLIM, *Surv. Geophy.* pp. 1–20. Published online, doi: 10.1007/s10712-011-9131-5.

Huybrechts, P. & Oerlemans, J. (1988). Evolution of the East Antarctic ice sheet: a numerical study of thermo-mechanical response patterns with changing climate, *Ann. Glaciol.* 11: 52–59.

Huybrechts, P., Payne, T. & the EISMINT intercomparison group (1996). The EISMINT benchmarks for testing ice sheets models, *Ann. Glaciol.* 23: 1–12.

Jansson, P., Hock, R. & Schneider, T. (2003). The concept of glacier storage: a review, *J. Hydrol.* 282(1–4): 116–129.

Jarosch, A. (2008). Icetools: a full stokes finite element model for glaciers, *Comput. Geosci.* 34: 1005–1014.

Jenssen, D. (1977). A three-dimensional polar ice-sheet model, *J. Glaciol.* 18(80): 373–389.

Jóhannesson, T., Raymond, C. & Waddington, E. (1989). Time-scale for adjustment of glaciers to changes in mass balance, *J. Glaciol.* 35(121): 355–369.

Jouvet, G., Picasso, M., Rappaz, J. & Blatter, H. (2008). A new algorithm to simulate the dynamics of a glacier: theory and applications, *J. Glaciol.* 54(188): 801–811.

Kaser, G. (2001). Glacier-climate interaction at low latitudes, *J. Glaciol.* 47(157): 195–204.

Kirschvink, J. (1992). Late Proterozoic low-latitude global glaciation: the snowball earth, *in* J. W. Schopf & C. Klein (eds), *The Proterozoic Biosphere*, Cambridge Univ. Press, Cambridge, pp. 51–52.

Krabill, W., Frederick, E., Manizade, S., Martin, C., Sonntag, J., Swift, R., Thomas, R., Wright, W. & Yungel, J. (1999). Rapid thinning of parts of the southern greenland ice sheet, *Science* 283(5407): 1522–1524.

Le Meur, E., Gagliardini, O., Zwinger, T. & Ruokolainen, J. (2004). Glacier flow modeling: a comparison of the shallow ice approximation and the full-stokes solution, *CR Physique* 5: 709–722.

Leclercq, P., Oerlemans, J. & Cogley, J. (2011). Estimating the glacier contribution to sea-level rise for the period 1800-2005, *Surv. Geophy.* pp. 1–17. Published online, doi: 10.1007/s10712-011-9121-7.

Lemke, P., Ren, J., Alley, R., Allison, I., Carrasco, J., Flato, G., Fujii, Y., Kaser, G., Mote, P., Thomas, R. & Zhang, T. (2007). Observations: Changes in snow, ice and frozen ground, *in* S. Solomon & 7 others (eds), *Climate Change 2007: The Physical Science Basis. Contribution of WG I to the Fourth Assessment Report of the IPCC*, Cambridge Univ. Press, Cambridge, pp. 337–383.

Leysinger Vieli, G. & Gudmundsson, G. (2004). On estimating length fluctuations of glaciers caused by changes in climate forcing, *J. Geophys. Res.* 109: F0 1007.

Lythe, M., Vaughan, D. & the BEDMAP Group (2001). BEDMAP: a new ice thickness and subglacial topographic model of Antarctica, *J. Geophys. Res.* 106(B6): 11335–11351.

MacAyeal, D. (1989). Large-scale ice flow over a viscous basal sediment: Theory and application to Ice Stream B, Antarctica, *J. Geophys. Res.* 94(B4): 4071–4087.

Mahaffy, M. (1976). A three-dimensional numerical model of ice sheets: tests on the Barnes Ice Cap, Northwest Territories, *J. Geophys. Res.* 81(6): 1059–1066.

Marshall, S. (2005). Recent advances in understanding ice sheet dynamics, *Earth Planet Sc. Lett.* 240: 191–204.

Marshall, S. & Clarke, G. (1997). A continuum mixture model of ice stream thermomechanics in the Laurentide Ice Sheet 1. Theory, *J. Geophys. Res.* 102(B9): 20599–20613.

Meier, M. (1984). Contribution of small glaciers to global sea level, *Science* 226(4681): 1418–1421.

Morland, L. (1984). Thermo mechanical balances of ice sheet flows, *Geophys. Astrophys. Fluid Dyn.* 29(1–4): 237–266.

Morland, L. & Staroszczyk, R. (2003). Strain-rate formulation of ice fabric evolution, *Ann. Glaciol.* 37: 35–39.

Nye, J. (1952). The mechanics of glacier flow, *J. Glaciol.* 2(12): 82–93.

Nye, J. (1953). The flow law of ice from measurements in glacier tunnels, laboratory experiments and the Jungfraufirn borehole experiment, *Proc. R. Soc. London, Ser. A* 219(1139): 477–489.

Nye, J. (1959). The motion of ice sheets and glaciers, *J. Glaciol.* 3(26): 493–507.

Nye, J. (1965). The flow of a glacier in a channel of rectangular, elliptical or parabolic cross-section, *J. Glaciol.* 5(41): 661–690.

Oerlemans, J. (1982). A model of the Antarctic ice sheet, *Nature* 297(5867): 550–553.

Oerlemans, J. (2005). Extracting a climate signal from 169 glacier record, *Science* 308(5722): 675–677.

Oerlemans, J., Anderson, B., Hubbard, A., Huybrechts, P., Jóhannesson, T., Knap, W., Schmeits, M., Stroeven, A., de Wal, R. V., Wallinga, J. & Zuo, Z. (1998). Modelling the response of glaciers to climate warming, *Clim. Dynam.* 14: 267–274.

Ohmura, A. (2004). Cryosphere during the twentieth century, *in* R. Sparks & C. Hawkesworth (eds), *The state of the planet: Frontiers and challenges in geophysics*, Geophysical monograph 150, pp. 239–257.

Paterson, W. & Budd, W. (1982). Flow parameters for ice-sheet modeling, *Cold Reg. Sci. Technol.* 6: 175–177.

Pattyn, F. (2003). A new three-dimensional higher-order thermomechanical ice sheet model: basic sensitivity, ice stream development, and ice flow across subglacial lakes, *J. Geophys. Res.* 108: B82382.

Pattyn, F., Perichon, L. & 19 others (2008). Benchmark experiments for higher-order and full-stokes ice sheet models (ISMIP-HOM), *The Cryosphere* 2: 95–108.

Payne, A., Huybrechts, P. & 9 others (1996). Results from the EISMINT model intercomparison: the effects of thermomechanical coupling, *J. Glaciol.* 46(153): 227–238.

Picasso, M., Rappaz, J. & Reist, A. (2008). Numerical simulation of the motion of a three-dimensional glacier, *Ann. Math. Blaise Pascal* 15: 1–28.

Price, S., Waddington, E. & Conway, H. (2007). A full-stress, thermomechanical flow band model using the finite volume method, *J. Geophys. Res.* 112(F3): F03020.

Rao, S. (2005). *The Finite Element Method in Engineering*, Elsevier Butterworth–Heinemann.

Raper, S. & Braithwaite, R. (2006). Low sea level rise projections from mountain glaciers and icecaps under global warming, *Nature* 439: 311–313.

Rigsby, G. (1958). Effect of hydrostatic pressure on the velocity of shear deformation of single ice crystals, *J. Glaciol.* 3: 273–278.

Robin, G. (1955). Ice movement and temperature distribution in glaciers and ice sheets, *J. Glaciol.* 2(18): 523–532.

Sargent, A. & Fastook, J. (2010). Manufactured analytical solutions for isothermal full-stokes ice sheet models, *The Cryosphere* 4: 285–311.

Shoemaker, E. & Morland, L. (1984). A glacier flow model incorporating longitudinal deviatoric stress, *J. Glaciol.* 30(106): 334–340.

Souček, O. & Martinec, Z. (2008). Iterative improvement of the shallow-ice approximation, *J. Glaciol.* 54(188): 812–822.

Thompson, L., Mosley-Thompson, E., Davis, M., Lin, P.-N., Henderson, K. & Mashiotta, T. (2003). Tropical glacier and ice core evidence of climate change on annual to millennial time scales, *Climatic Change* 59: 137–155.

Van der Veen, C. (1999). *Fundamentals of Glacier Dynamics*, AA Balkema, Rotterdam.

Viviroli, D., Weingartner, R. & Messerli, B. (2003). Assessing the hydrological significance of the world's mountains, *Mt. Res. Dev.* 23: 32–40.

Waddington, E. (2010). Life, death and afterlife of the extrusion flow theory, *J. Glaciol.* 56(200): 973–996.

Wang, W. & Warner, R. (1999). Modelling of anisotropic ice flow in Law Dome, East Antarctica, *Ann. Glaciol.* 29: 184–190.

Weertman, J. (1973). Creep of ice, *in* E. Whalley, S. Jones & L. Gold (eds), *Physics and Chemistry of Ice*, Royal Society of Canada, Ottawa, pp. 320–337.

Whillans, I. (1987). Force budget of ice sheets, *in* C. Van der Veen & J. Oerlemans (eds), *Dynamics of the West Antarctic Ice Sheet*, Reidel Publ. Co., Dordrecht, pp. 17–36.

Whillans, I. & Van der Veen, C. (1997). The role of lateral drag in the dynamics of Ice Stream B, Antarctica, *J. Glaciol.* 43(144): 231–237.

Zemp, M., Haeberli, W., Hoelzle, M. & Paul, F. (2006). Alpine glaciers to disappear within decades?, *Geophys. Res. Lett* 33: L13504.

Zwinger, T., Greve, R., Gagliardini, O., Shiraiwa, T. & Lyly, M. (2007). A full stokes-flow thermo-mechanical model for firn and ice applied to the Gorshkov crater glacier, Kamchatka, *Ann. Glaciol.* 45: 29–37.

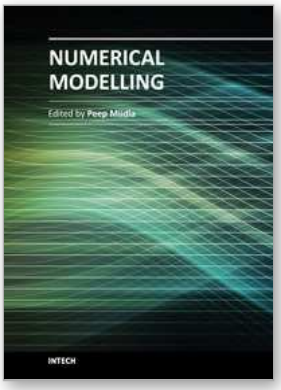

Numerical Modelling

Edited by Dr. Peep Miidla

ISBN 978-953-51-0219-9
Hard cover, 398 pages
Publisher InTech
Published online 23, March, 2012
Published in print edition March, 2012

This book demonstrates applications and case studies performed by experts for professionals and students in the field of technology, engineering, materials, decision making management and other industries in which mathematical modelling plays a role. Each chapter discusses an example and these are ranging from well-known standards to novelty applications. Models are developed and analysed in details, authors carefully consider the procedure for constructing a mathematical replacement of phenomenon under consideration. For most of the cases this leads to the partial differential equations, for the solution of which numerical methods are necessary to use. The term Model is mainly understood as an ensemble of equations which describe the variables and interrelations of a physical system or process. Developments in computer technology and related software have provided numerous tools of increasing power for specialists in mathematical modelling. One finds a variety of these used to obtain the numerical results of the book.